Spectroscopic properties and quantum cutting in Tb3+–Yb3+ co-doped ZrO2 nanocrystals

I. A. A. Terra, L. J. Borrero-González, J. M. Carvalho, M. C. Terrile, M. C. F. C. Felinto, H. F. Brito, and L. A. O. Nunes
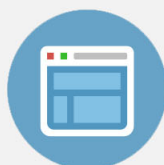
Spectroscopic properties and quantum cutting in Tb^{3+}–Yb^{3+} co-doped ZrO$_2$ nanocrystals

I. A. A. Terra,[1] L. J. Borrero-González,[1,a)] J. M. Carvalho,[2] M. C. Terrile,[1] M. C. F. C. Felinto,[3] H. F. Brito,[2] and L. A. O. Nunes[1]

[1]*Instituto de Física de São Carlos, Universidade de São Paulo, CP 369, 13560-970 São Carlos, SP, Brazil*
[2]*Instituto de Química, Universidade de São Paulo, Av. Prof. Lineu Prestes, 748, 05508-900 São Paulo, SP, Brazil*
[3]*Instituto de Pesquisas Energéticas e Nucleares, Av. Prof. Lineu Prestes, 2242, 05508-000 São Paulo, SP, Brazil*

Ultraviolet-visible to near-infrared quantum cutting (QC) materials are a promising tool to enhance the efficiency of conventional crystalline silicon solar cells. The spectroscopic properties of Tb^{3+}–Yb^{3+} co-doped ZrO$_2$ nanocrystals are presented, and the QC mechanisms in these nanocrystals are investigated. The materials were fabricated using the sol gel method and characterized using X-ray powder diffraction, X-ray absorption near edge structure, and luminescence spectroscopy. The incorporation of Yb^{3+} ions into the host induced a crystalline phase change of ZrO$_2$ from monoclinic to tetragonal to cubic symmetry and influenced the Tb valence state. The Tb^{3+} visible emission, excitation intensity (monitored by the Tb^{3+}:^{5}D$_4$ emission), decay time of the Tb^{3+}:^{5}D$_4$ emitter level, and down-conversion (DC) emission intensity increased with Yb^{3+} concentration. Furthermore, a sublinear dependence of the DC intensity on the excitation power at the Tb^{3+}:^{5}D$_4$ level indicated the coexistence of two different QC mechanisms from Tb$^{3+} \rightarrow$ Yb^{3+}. The first one is a linear process in which one Tb^{3+} ion transfers its energy simultaneously to two Yb^{3+} ions, known as cooperative energy transfer, and the second one is a non-linear process involving an intermediated virtual level in the Tb^{3+} ion. © *2013 American Institute of Physics.* [http://dx.doi.org/10.1063/1.4792743]

I. INTRODUCTION

Developing a quantum cutting (QC) material that efficiently converts energy from the ultraviolet (UV)-visible (VIS) region of the solar spectrum to the near-infrared (NIR), where a single-junction crystalline silicon solar cell has a strong spectral response, presents a great challenge to fabricate more efficient photovoltaic devices. Shockley and Queisser[1] reported a theoretical efficiency limit of ∼30% for a single-junction crystalline silicon solar cell. The spectral mismatch of the solar spectrum and the band gap at ∼1.1 eV of crystalline silicon are the major issues that restrict this efficiency. The photons with energies smaller than the band gap are not absorbed (transmission losses), and a large portion of the energy of the photons with energies exceeding the band gap is lost as heat of the charge carries (thermalization losses).[2] Trupke *et al.*[3] reported that the thermalization losses could be minimized when a QC material is placed in front of a single-junction crystalline silicon solar cell, achieving a conversion efficiency of up to 38.6%. Recently, several authors have studied the use of rare-earth ion doped materials as quantum cutters to improve this efficiency.[4–6] Ion couples such as Nd^{3+}–Yb^{3+}, Pr^{3+}–Yb^{3+}, Er^{3+}–Yb^{3+}, and Tb^{3+}–Yb^{3+}, appear promising for this purpose[6–16] because the Nd^{3+}, Pr^{3+}, Er^{3+}, and Tb^{3+} ions absorb in the UV-VIS region and then transfer the energy to Yb^{3+} ions that emit in the NIR at ∼1000 nm. The combination of Tb^{3+} (sensitizer)

and Yb^{3+} (activator) ions is particularly interesting because the Tb^{3+}:^{5}D$_4 \rightarrow$ ^{7}F$_6$ transition occurs at 488 nm, approximately twice the energy of the Yb^{3+}:^{2}F$_{7/2} \rightarrow$ ^{7}F$_{5/2}$ absorption.

Quantum efficiencies higher than 100% have been reported in the literature for the Tb^{3+}–Yb^{3+} system.[5,13–15,17–27] However, the QC mechanism involved in this system is still debated. Some authors[13] have found that the down-conversion (DC) intensity has a linear relation to the excitation power in a double logarithmic plot with a slope of 1, while others[27] have observed a sublinear relation with a slope of 0.49. Interestingly, Strek *et al.*[28] were able to control the slope through the temperature; they observed a slope of 0.45 at 300 K and 0.88 at 77 K. Based on these reports, the QC may be either a linear or a sublinear process, indicating different energy transfer mechanisms responsible for the QC in the Tb^{3+}–Yb^{3+} system. More recently, Duan *et al.*[29] attempted to elucidate the origin of the QC in NaYF$_4$:Tb^{3+}, Yb^{3+} powder samples by invoking two different energy transfer mechanisms from Tb^{3+} to Yb^{3+} to explain the observed linear and sublinear slopes.

Zirconia (ZrO$_2$) is an excellent material for use in optics owing to its hardness, optical transparency, thermal and chemical stability, high refractive index (2.15–2.18),[30–32] and wide band gaps of 5.0 and 5.8 eV for monoclinic-ZrO$_2$ and tetragonal-ZrO$_2$, respectively.[33] The stretching frequency of the Zr-O bond is approximately 470 cm^{-1}, which is much lower than that of Al-O (870 cm^{-1}) or Si-O (1100 cm^{-1}).[34] This low energy phonon opens up the possibility of efficient luminescence of active ions incorporated

a)Author to whom correspondence should be addressed. Electronic mail: lborrero@ursa.ifsc.usp.br.

into the ZrO_2 matrix. In addition, zirconia displays a well-known polymorphism with three different crystalline structures: cubic (c-ZrO_2), tetragonal (t-ZrO_2), and monoclinic (m-ZrO_2).[35] The crystalline structure of ZrO_2 is also known to change with the thermal treatment and with the incorporation of rare-earth ions.[36]

The purpose of this paper is to investigate the spectroscopic properties and the quantum cutting mechanisms in Tb^{3+}–Yb^{3+} co-doped ZrO_2 nanocrystals. The samples were produced using the sol-gel method. They were characterized using X-ray powder diffraction (XRD), X-ray absorption near edge structure (XANES), electron spin resonance (EPR), and luminescence spectroscopy. As the Yb^{3+} concentration increased, the XRD measurements revealed a crystalline phase change of ZrO_2 from monoclinic to tetragonal to cubic. The XANES measurements revealed a change of the Tb valence state as Yb^{3+} was incorporated. The Tb^{3+} visible emission, excitation intensity (monitored via the Tb^{3+}:$^5D_4$ emission) and the decay time of the Tb^{3+}:$^5D_4$ emitter level increased with Yb^{3+} concentration. In addition, DC emission was observed at high Yb^{3+} concentration. Finally, a sublinear dependence of the DC intensity on the excitation power at the Tb^{3+}:$^5D_4$ level indicated the coexistence of two different QC mechanisms for $Tb^{3+} \rightarrow Yb^{3+}$.

II. EXPERIMENTAL DETAILS

A. Material synthesis

A series of ZrO_2:1Tb + xYb co-doped materials with ($x = 0$, 1, 5, 10, and 20 mole-% and a ZrO_2:1 Tb+20 Gd material were prepared using a one-step sol-gel method.[36] The as-prepared materials were thermally treated for 5 h at 1000 °C to obtain the co-doped ZrO_2 nanocrystals, as described previously.[37,38]

B. Material characterizations

The thermally treated samples were structurally characterized using XRD, performed on a Rigaku-Miniflex II diffractometer with $CuK_{\alpha 1}$ radiation (1.5406 Å) in the 2θ range of 20–70°.

The valence state of Tb was evaluated by performing XANES spectroscopy on the ZrO_2:1 Tb + xYb ($x = 1$, 5, 10, and 20 mole-%) as-prepared and thermally treated samples using the beam line XAFS1 at Laboratório Nacional de Luz Sincrotron (LNLS) in Campinas, Brazil. The data were collected in the fluorescence mode over the Tb L_{III} edge. A freshly annealed terbium oxide (Tb_4O_7) was used as the reference sample.

In addition, EPR spectra of the ZrO_2:1 Tb + xYb samples ($x = 1$, 5, 10, and 20 mole-%) were recorded using a Bruker Ele Xsys, E 580 X band (9 GHz) spectrometer to confirm the change of the Tb valence with the Yb^{3+} incorporation.

Photoluminescence (PL) spectra in the visible and infrared were obtained using an HeCd laser (Kimmon/IK5652R-G) at 325 nm and an Argon laser at 488 nm (Spectra physics 166) as excitation sources. The luminescent signals were dispersed by a monochromator (0.3 m, Thermo Jarrel Ash/82497),

detected by either a photomultiplier tube (Hamamatsu PMT/R928) or an InGaAs detector and amplified by a lock-in.

Photoluminescence excitation (PLE) measurements in the 460–510 nm range (monitoring at 544 nm) were made on an SPEX Fluorolog spectrofluorometer (0.22 m, SPEX/1680) equipped with an Xe-lamp as the excitation source and a PMT/R928 for detection.

Luminescence decay curves for the Tb^{3+}:$^5D_4 \rightarrow {}^7F_5$ and Yb^{3+}:$^2F_{5/2} \rightarrow {}^2F_{7/2}$ transitions were obtained using an optical parametric oscillator (OPO) (Surelite SLOP/Continumm) pumped by the third harmonic from an Nd:YAG laser (Surelite SLII-10/Continumm, 355 nm, 5 ns, 10 Hz). The luminescent signals of both Tb^{3+} and Yb^{3+} were dispersed by the monochromator (0.3 m). The PMT/R928 was used to detect the decay time of the Tb^{3+} and another photomultiplier tube (Hamamatsu/R632) was used to measure the decay curves of the Yb^{3+}. The signals were registered on a digital oscilloscope (TekTronix/TDS380). The decay times of both the Tb^{3+}:$^5D_4 \rightarrow {}^7F_5$ and the Yb^{3+}:$^2F_{5/2} \rightarrow {}^2F_{7/2}$ transitions were measured as a function of the Yb^{3+} concentration.

The excitation power dependent measurements were carried out using an Argon laser at 488 nm (Spectra physics 166) in the range 50-200 mW, monitoring the DC emission from Yb^{3+}:$^2F_{5/2} \rightarrow {}^2F_{7/2}$ (at 980 nm).

All of the material characterizations were carried out at room temperature.

III. RESULTS AND ANALYSIS

A. XRD and XANES characterization

The crystalline structures of the ZrO_2:1Tb+xYb annealed samples ($x = 1$, 5, 10, and 20 mole-%) were determined using XRD measurements, and the results are shown in Figure 1. For the ZrO_2:1 Tb+1 Yb material, the dominant structure is the monoclinic phase. However, owing to the incorporation of Yb^{3+} ions, the tetragonal (for 1 to 5 mole-% of Yb^{3+}) and cubic phases (for 10 to 20 mole-% of Yb^{3+}) are stabilized. Some authors have reported a crystalline phase change from monoclinic to tetragonal to cubic with RE^{3+} incorporation.[39,40] The radii of RE^{3+} (0.985/CN:8 and 1.040 Å/CN: 8 for the Yb^{3+} and Tb^{3+} ions, respectively) are larger than the radius of Zr^{4+} (0.84 Å/CN:8):[41] the incorporation of such ions induces expansion of the ZrO_2 lattice as well as the creation of oxide vacancies owing to charge compensation.[11] To avoid collapse of the structure, the lattice then stabilizes in the tetragonal or cubic phases.

The average crystallite sizes were calculated using the Scherrer equation,[11] and values in the 21–44 nm range were obtained for Yb^{3+} concentrations of $x = 1$ to 20 mole-%. This fact is attributed to varying cation concentrations in the precursor solution, leading to different hydrolysis rates for the different materials and consequent large variations in the agglomeration of the particles.

The XANES measurement is the most direct method of evaluating the valence change for rare earth ions.[42] The XANES spectra of the Tb (L_{III}) absorption edge of the as-prepared and annealed ZrO_2:1 Tb + xYb ($x = 1$, 5, 10, and 20 mole-%) samples were recorded. The normalized spectra for $x = 1$ and 20 mole-% are shown in Figure 2(a) for the

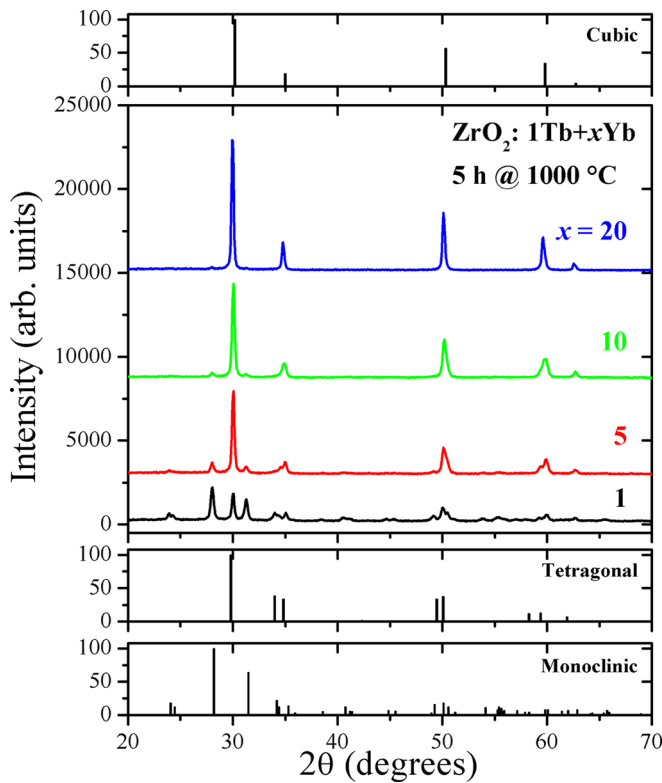FIG. 1. XRD patterns of the ZrO_2:1 Tb + xYb annealed samples ($x = 1, 5,$ 10, and 20 mole-%). The vertical bars indicate the standard ICDD, PDF data for the 36-0460 (monoclinic ZrO_2), 42-1164 (tetragonal ZrO_2), and 081-1550 (cubic ZrO_2) phases.

as-prepared samples and in Figure 2(b) for the annealed (5 h at 1000 °C) samples. The spectrum of the Tb_4O_7 (reference) sample is also shown for comparison. The reference spectrum has two peaks at 7510 and 7518 eV associated with the Tb^{3+} and Tb^{4+} valence states, respectively, in agreement with Tb_4O_7 spectra in the literature.[42] In Figure 2(a), the as-prepared samples show only the Tb^{3+} peak because all of the samples were synthesized using Tb^{3+} nitrate as the precursor. After annealing, Tb oxidation was observed at low Yb^{3+}
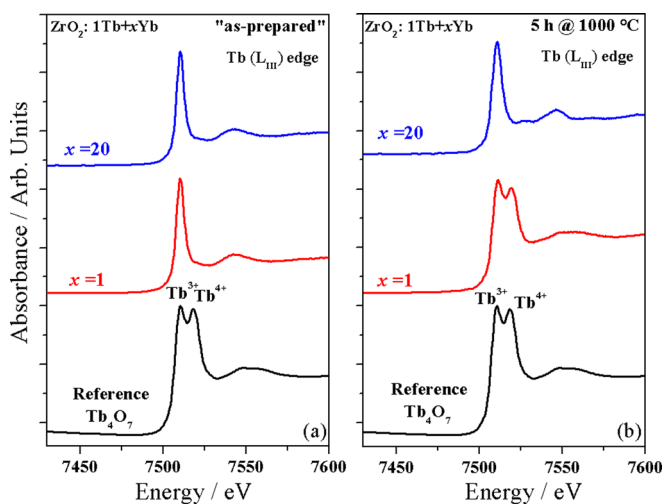
concentration, promoting a Tb valence conversion from Tb^{3+} to Tb^{4+}. However, at high Yb^{3+} concentration, Tb oxidation is inhibited. This inhibition could be explained by the contribution of the oxygen vacancies generated by Yb co-doping, which must be accounted for in the redox chemistry of the Tb ion.

A decrease in the Tb^{4+} concentration with increasing Yb^{3+} concentration was confirmed by performing EPR spectroscopy on the ZrO_2:1 Tb+xYb annealed samples ($x = 1, 5,$ 10, and 20 mole-%) (results not shown here). These measurements indicated a Tb valence conversion from Tb^{4+} to Tb^{3+}, in agreement with the XANES data.

The influence of crystalline structural changes and the Tb valence conversion on the luminescent properties of the ZrO_2:1 Tb + xYb annealed samples will be analyzed in detail in Sec. III B.

B. Luminescence characterization

The energy level diagrams of the Tb^{3+} and Yb^{3+} ions are shown in Figure 3, along with the relevant optical transitions. Two different QC mechanisms from Tb^{3+} to Yb^{3+} are also shown.

The visible luminescence spectra of the ZrO_2:1 Tb + xYb ($x = 1, 5, 10,$ and 20 mole-%) annealed samples under 325 nm excitation are shown in Figure 4. The emission peaks, corresponding to the optical transitions ($^5D_4 \rightarrow {}^7F_J$) of the Tb^{3+} ion occur at approximately 490 nm ($^5D_4 \rightarrow {}^7F_6$), 544 nm ($^5D_4 \rightarrow {}^7F_5$), 587 nm ($^5D_4 \rightarrow {}^7F_4$), and 622 nm ($^5D_4 \rightarrow {}^7F_3$). A bright white-blue luminescence centered at 500 nm is also observed for the ZrO_2:1 Tb + 1 Yb sample. The intensity of this broad-band luminescence was strongly suppressed with increasing Yb^{3+} concentration. This broad-band luminescence of non-doped ZrO_2 was suggested to result from a Ti impurity in ZrO_2 in previous work.[37] The

FIG. 2. Normalized XANES spectra of the as-prepared (a) and annealed (b) ZrO_2:1 Tb + xYb ($x = 1$ and 20 mole-%) materials. For comparison, the spectrum of the Tb_4O_7 material is also shown. The spectra were recorded on the Tb (L_{III}) edge.
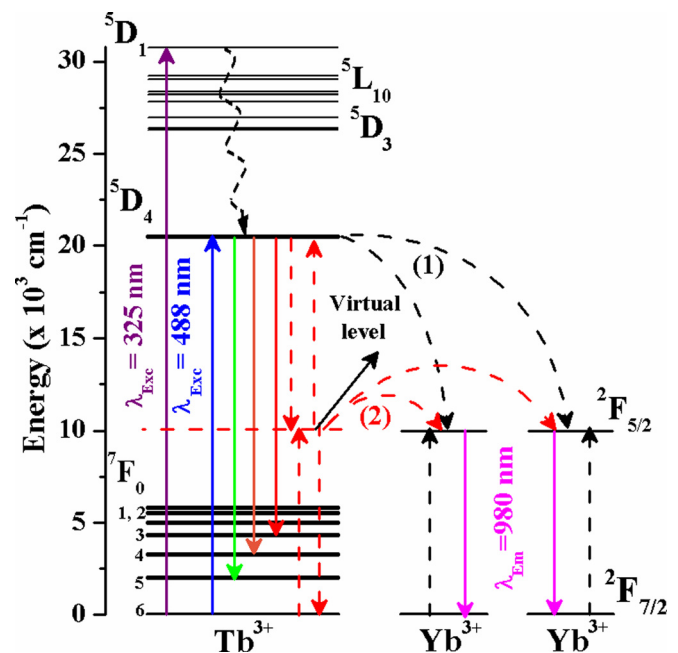

FIG. 3. Energy level diagram of the Tb^{3+} and Yb^{3+} ions. The energy transfer mechanisms of the quantum cutting under Tb^{3+} excitation are shown. (1) CET and (2) energy transfer via intermediate virtual level.
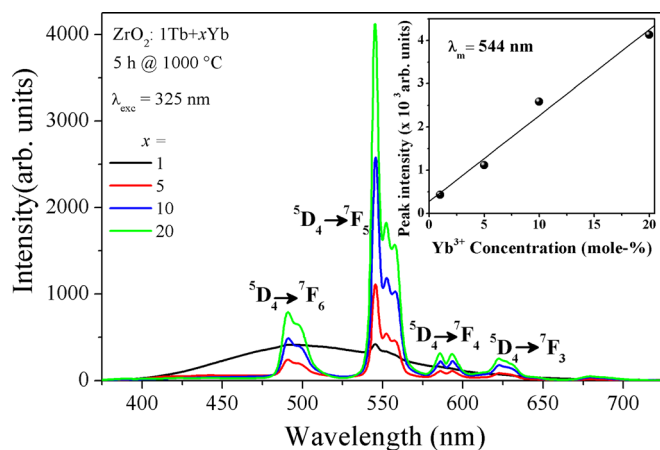
FIG. 4. Visible emission spectra of the ZrO_2:1 Tb + xYb annealed samples ($x = 1$, 5, 10, and 20 mole-%) under excitation at 325 nm. The inset shows the peak emission intensity of the Tb^{3+}:$^5D_4 \to {}^7F_5$ transition, monitored at $\lambda_m = 544$ nm as a function of the Yb^{3+} concentration.

inset in Figure 4 shows an increase in the peak emission intensity at 544 nm as a function of the Yb^{3+} concentration, explained by an increase in the Tb^{3+} ion concentration.

PLE spectra are useful for investigating the absorption mechanism responsible for the Tb^{3+}-related emissions. Figure 5 shows the excitation spectra of the ZrO_2:1 Tb + xYb annealed samples ($x = 1$, 5, 10, and 20 mole-%) excited with an Xe-lamp, monitoring the Tb^{3+}:$^5D_4 \to {}^7F_5$ transition ($\lambda_m = 544$ nm). The spectra clearly display a band centered at 485 nm related to the Tb^{3+} absorption structure from the ground energy level, $^7F_6$ to $^5D_4$. The intensity increases with Yb^{3+} doping, and this result confirms an increase of the Tb^{3+} ion concentration, in agreement with the XANES, EPR data, and the visible luminescence.

The luminescence decay times were obtained, and a correlation with the effect of increasing the Tb^{3+} concentration and crystal structure is demonstrated below.

Figure 6 shows the luminescence decay times of the ZrO_2:1 Tb + xYb annealed samples as a function of the Yb^{3+} concentration after excitation with a pulsed laser ($\lambda_{exc} = 355$ nm, 5 ns), monitoring the Tb^{3+}:$^5D_4 \to {}^7F_5$ transition at 544 nm. The decay time increases with the Yb^{3+}
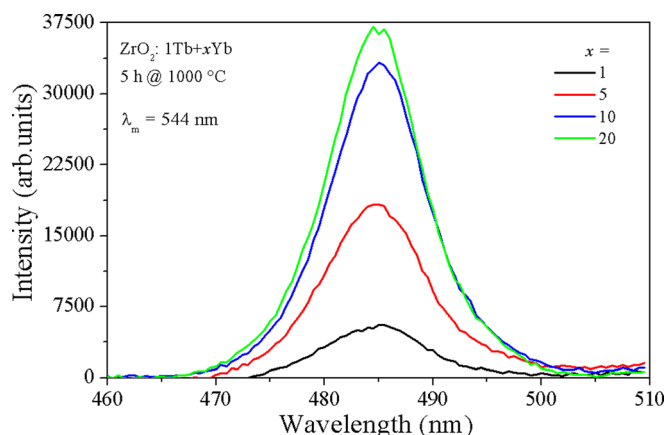

FIG. 5. PLE spectra of the ZrO_2:1 Tb + xYb annealed samples ($x = 1$, 5, 10, and 20 mole-%) excited with an Xe-lamp, monitoring the Tb^{3+}:$^5D_4 \to {}^7F_5$ transition ($\lambda_m = 544$ nm).
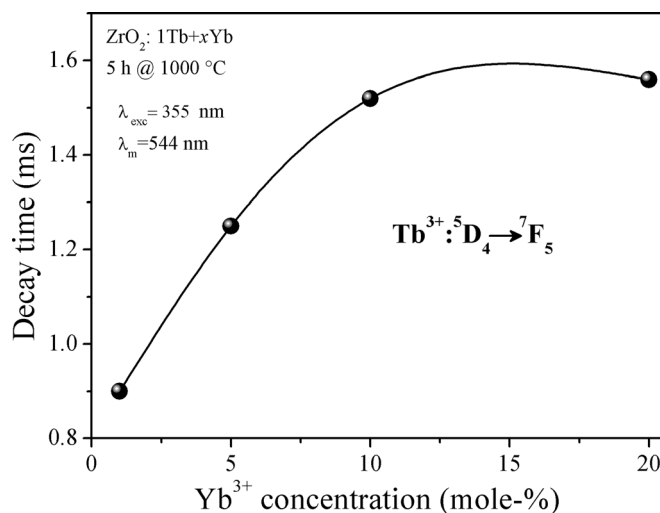

FIG. 6. Luminescence decay times of the ZrO_2:1 Tb + xYb annealed samples as a function of the Yb^{3+} concentration, after excitation with a pulsed laser ($\lambda_{exc} = 355$ nm, 5 ns), monitoring the Tb^{3+}:$^5D_4 \to {}^7F_5$ transition at 544 nm. The solid line is a visual guide.

doping. This increase in the decay time may be caused owing to the forbidden radiative stronger transitions arising from the increased symmetry of the crystal, in agreement with the XRD results.

To confirm the change in the crystal symmetry with the incorporation of RE^{3+} ions, we have measured the Tb^{3+}:$^5D_4$ decay time at 544 nm for ZrO_2:1Tb singly doped and ZrO_2:1 Tb + 20 Gd co-doped samples after excitation at 355 nm. The results are 0.98 ms and 2.27 ms for the ZrO_2:1Tb and ZrO_2:1 Tb + 20 Gd samples, respectively. This indicates that after the incorporation of Gd^{3+}, there is an increase in the crystal symmetry, consequently increasing the Tb^{3+}:$^5D_4$ decay time. At 355 nm, Gd^{3+} ions are optically passive and the effect on the forbidden radiative transitions owing to the high symmetry of the crystal can be investigated. On the other hand, the decay time for the ZrO_2:1Tb + 20Yb sample was considerable lower (1.56 ms, see Figure 6) than that for the ZrO_2:1Tb + 20Gd sample and this may owe to the occurrence of the DC process in the ZrO_2:1 Tb + 20 Yb sample. The DC process is also observed when comparing the decay times of 0.98 ms and 0.90 ms for the ZrO_2:1 Tb and ZrO_2:1 Tb + 1 Yb samples. In addition, it is important to mention that the ZrO_2:1 Tb + xYb samples display NIR emission (as will be shown below), indicating that QC mechanisms (see Figure 3) are responsible for the depopulation of the Tb^{3+}:$^5D_4$ level through a DC process from $Tb^{3+} \to Yb^{3+}$. The combination of these facts explains the observed behavior of the luminescence decay time of the Tb^{3+}:$^5D_4 \to {}^7F_5$ transition.

The NIR emission spectra of the ZrO_2:1 Tb + xYb annealed samples ($x = 1$, 5, 10, and 20 mole-%) after resonant pumping of the Tb^{3+}:$^5D_4$ level (at 488 nm) were recorded as a function of the Yb^{3+} doping (see Figure 7(a)). The NIR emission profile of the Yb^{3+} ions has three peaks centered at 981, 1012, and 1044 nm for the ZrO_2:1 Tb + 1 Yb annealed sample. However, with increasing Yb^{3+} concentration, the spectral profile changes from three to two peaks owing to the higher symmetry. Similar behavior was
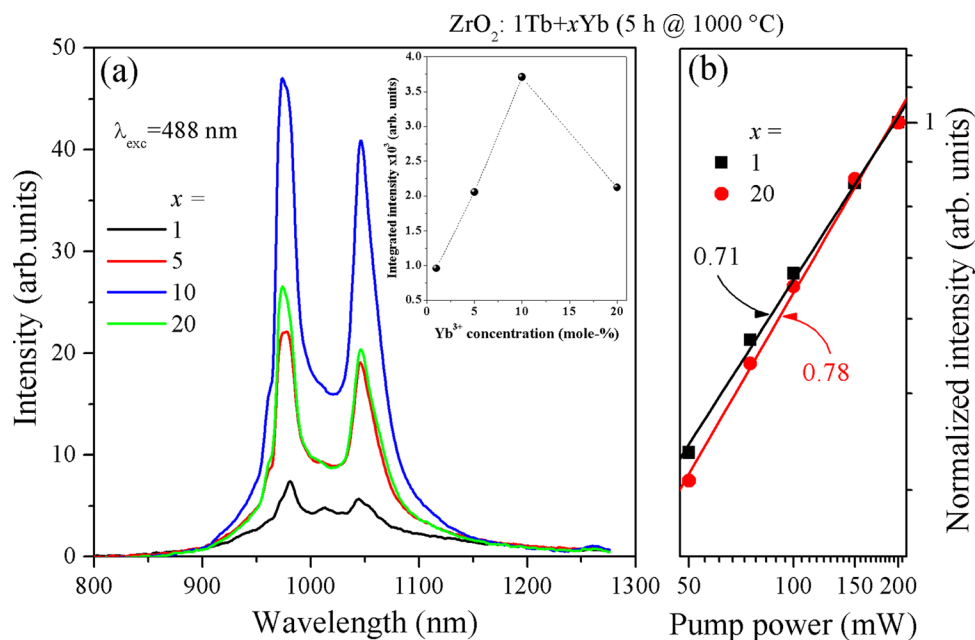
FIG. 7. NIR emission spectra of the ZrO_2:1 Tb + xYb annealed samples ($x = 1$, 5, 10, and 20 mole-%) under excitation at 488 nm. The inset shows the dependence of the Yb^{3+} emission intensity on the excitation power for the $^5D_4$ level of the Tb^{3+} ion, monitored at $\lambda_m = 980$ nm.

observed by de la Rosa *et al.*[39] in Yb^{3+} singly doped ZrO_2 nanocrystals. In addition, the NIR emission integrated intensity (see inset in Figure 7(a)) increases with Yb^{3+} doping from 1 to 10 mole-% owing to an DC process from Tb^{3+} to Yb^{3+}. However, at higher Yb^{3+} concentration (20 mole-%), there is a decrease in the DC intensity, which may be caused owing to the forbidden radiative stronger transitions arising from the increased symmetry of the crystal (cubic),[43] and Yb^{3+} concentration quenching. The Yb^{3+} concentration quenching is often observed in Yb doped materials at high Yb^{3+} concentrations.[44]

Excitation power measurements were performed to elucidate the origin of the mechanisms involved in the DC process. The power dependence curves for the DC emission Yb^{3+}:$^2F_{5/2} \rightarrow {}^2F_{7/2}$ (at 980 nm) in the range 50–200 mW were recorded for all of the annealed samples. Figure 7(b) shows a double logarithmic plot of the linear fits to the dependence of the NIR emission intensity at 980 nm on the excitation power after resonant pumping of the Tb^{3+}:$^5D_4$ level (at 488 nm) for the annealed samples with $x = 1$ and 20 mole-% Yb^{3+}. The slope increases from 0.71 to 0.78 as the Yb^{3+} concentration increases. Duan *et al.*[29] obtained similar slopes between 0.7 and 0.8 depending on the Yb^{3+} concentration in $NaYF_4$:Tb^{3+}, Yb^{3+} powder samples. Interestingly, sublinear slopes of 0.45 (300 K) and 0.88 (77 K) were also reported by Strek *et al.*[28] in Tb^{3+}–$KYb(WO_4)_2$ crystal. However, the physical meaning of theses slopes is poorly discussed in the literature. More recently, Duan *et al.*[29] developed a QC model, using rate equations to explain the sublinear slopes, in which the slopes were attributed to the coexistence of two different QC mechanisms: a linear process, in which the DC intensity varies linearly with the excitation power (slope of 1), where the energy transfer is from one Tb^{3+} ion to two Yb^{3+} ions (referred to as the cooperative energy transfer process (1) in Figure 3) and a nonlinear process, in which the DC intensity varies as the square root of the excitation power (slope of 0.5), where the energy transfer is from one Tb^{3+} ion to two Yb^{3+} ions mediated by

a virtual level (referred to as energy transfer via intermediate virtual level process (2) in Figure 3). Following the reasoning of Duan *et al.*, our sublinear slopes indicate the coexistence of the aforementioned processes. We are currently performing a systematic study of different materials to elucidate the nature of these sublinear slopes and will report the results in future work.

IV. CONCLUSIONS

In conclusion, our results demonstrated that Yb^{3+} ion incorporation strongly influences the spectroscopic properties of Tb^{3+}–Yb^{3+} co-doped zirconia nanocrystals. A change of the crystalline phase from monoclinic to tetragonal to cubic, and an increase in the Tb^{3+} ion concentration were observed with increasing Yb^{3+} concentration. As a consequence of the high symmetry of the crystal, the Tb^{3+}:$^5D_4$ level decay time increased. The DC emission was also observed, with the 10 mole-% Yb sample displaying the highest DC emission. The DC emission owes to a coexistence of two QC mechanisms: a linear and a non-linear process, which explains the sublinearity of the slopes of the DC intensity versus the excitation power. Our results suggest that Tb^{3+}–Yb^{3+} co-doped ZrO_2 nanocrystals have potential as a QC material for solar cells.

[1]W. Shockley and H. J. Queisser, J. Appl. Phys. **32**, 510 (1961).

[2]B. S. Richards, Sol. Energy Mater. Sol. Cells **90**, 1189 (2006).

[3]T. Trupke, M. A. Green, and P. Würfel, J. Appl. Phys. **92**, 1668 (2002).

[4]B. M. van der Ende, L. Aarts, and A. Meijerink, Phys. Chem. Chem. Phys. **11**, 11081 (2009).

[5]P. Vergeer, T. Vlugt, M. Kox, M. den Hertog, J. van der Eerden, and A. Meijerink, Phys. Rev. B **71**, 014119 (2005).

[6]J. J. Eilers, D. Biner, J. van Wijngaarden, K. Krämer, H. U. Guüdel, and A. Meijerink, Appl. Phys. Lett. **96**, 151106 (2010).

[7]D. Chen, Y. Yu, H. Lin, P. Huang, Z. Shan, and Y. Wang, Opt. Lett. **35**, 220 (2010).

[8]L. J. Borrero-González and L. A. O. Nunes, J. Phys.: Condens. Matter. **24**, 385501 (2012).

[9]D. Chen, Y. Wang, Y. Yu, P. Huang, and F. Weng, Opt. Lett. **33**, 1884 (2008).

[10]E. De la Rosa-Cruz, L. A. Díaz-Torres, R. A. Rodríguez-Rojas, M. A. Meneses-Nava, O. Barbosa-García, and P. Salas, Appl. Phys. Lett. **83**, 4903 (2003).

[11]G. Chen, G. Somesfalean, Y. Liu, Z. Zhang, Q. Sun, and F. Wang, Phys. Rev. B **75**, 195204 (2007).

[12]I. Hyppänen, J. Hölsä, J. Kankare, M. Lastusaari, and L. Pihlgren, Ann. N. Y. Acad. Sci. **1130**, 267 (2008).

[13]S. Ye, Y. Katayama, and S. Tanabe, J. Non-Cryst. Solids **357**, 2268 (2011).

[14]Q. Duan, F. Qin, D. Wang, W. Xu, J. Cheng, Z. Zhang, and W. Cao, J. Appl. Phys. **110**, 113503 (2011).

[15]S. Ye, B. Zhu, J. Chen, J. Luo, and J. R. Qiu, Appl. Phys. Lett. **92**, 141112 (2008).

[16]I. A. A. Terra, L. J. Borrero-González, T. R. Figueredo, J. M. P. Almeida, A. C. Hernandes, L. A. O. Nunes, and O. L. Malta, J. Lumin. **132**, 1678 (2012).

[17]P. Molina, V. Vasyliev, E. G. Víllora, and K. Shimamura, J. Appl. Phys. **110**, 123527 (2011).

[18]Q. Zhang, X. Liu, S. Ye, B. Zhu, Y. Qiao, G. Dong, B. Qian, and D. Chen, IEEE Photon. Technol. Lett. **21**, 1169 (2009).

[19]Q. Y. Zhang, C. H. Yang, and Y. X. Pan, Appl. Phys. Lett. **90**, 021107 (2007).

[20]Q. Y. Zhang, C. H. Yang, Z. H. Jiang, and X. H. Ji, Appl. Phys. Lett. **90**, 061914 (2007).

[21]Q. Y. Zhang, G. F. Yang, and Z. H. Jiang, Appl. Phys. Lett. **91**, 051903 (2007).

[22]X. Y. Huang and Q. Y. Zhang, J. Appl. Phys. **105**, 053521 (2009).

[23]J. L. Yuan, X. Y. Zeng, J. T. Zhao, Z. J. Zhang, H. H. Chen, and X. X. Yang, J. Phys. D: Appl. Phys. **41**, 105406 (2008).

[24]Y. Wang, L. Xie, and H. Zhang, J. Appl. Phys. **105**, 023528 (2009).

[25]G. Lakshminarayana and J. Qiu, J. Alloys Compd. **481**, 582 (2009).

[26]X. Liu, S. Ye, Y. Qiao, G. Dong, B. Zhu, D. Chen, G. Lakshminarayana, and J. Qiu, Appl. Phys. B **96**, 51 (2009).

[27]D. Chen, Y. Yu, Y. Wang, P. Huang, and F. Weng, J. Phys. Chem. C **113**, 6406 (2009).

[28]W. Strek, A. Bednarkiewicz, and P. J. Deren, J. Lumin. **92**, 229 (2001).

[29]Q. Duan, F. Qin, Z. Zhang, and W. Cao, Opt. Lett. **37**, 521 (2012).

[30]R. C. Garvie, R. H. Hannink, and R. T. Pascoe, Nature **258**, 703 (1975).

[31]P. Wright and A. G. Evans, Curr. Opin. Solid State Mater. Sci. **4**, 255 (1999).

[32]C. W. Li, M. M. McKerns, and B. Fultz, J. Am. Ceram. Soc. **94**, 224 (2011).

[33]A. Emeline, G. V. Kataeva, A. S. Litke, A. V. Rudakova, V. K. Ryabchuk, and N. Serpone, Langmuir **14**, 5011 (1998).

[34]I. Hyppanen, J. Holsa, J. Kankare, M. Lastusaari, L. Pihlgren, and T. Soukka, J. Fluoresc. **18**, 1029 (2008).

[35]T. Nguyen, Solid State Ionics **138**, 191 (2001).

[36]L. Li, H. K. Yang, B. K. Moon, B. C. Choi, J. H. Jeong, K. Jang, H. S. Lee, and S. S. Yi, J. Nanosci. Nanotechnol. **11**, 350 (2011).

[37]L. L. Hench and J. K. West, Chem. Rev. **90**, 33 (1990).

[38]J. M. Carvalho, L. C. V. Rodrigues, J. Hölsä, M. Lastusaari, L. A. O. Nunes, M. C. F. C. Felinto, O. L. Malta, and H. F. Brito, Opt. Mater. Express **2**, 331 (2012).

[39]E. De La Rosa, D. Solis, L. A. Díaz-Torres, P. Salas, C. Angeles-Chavez, and O. Meza, J. Appl. Phys. **104**, 103508 (2008).

[40]E. De La Rosa, L. Diaz Torres, P. Salas, and R. Rodriguez, Opt. Mater. **27**, 1320 (2005).

[41]R. D. Shannon, Acta Crystallogr., Sect. A: Cryst. Phys., Diffr., Theor. Gen. Crystallogr. **32**, 751 (1976).

[42]H. Arashi, S. Shin, H. Miura, A. Nakashima, and M. Ishigame, Solid State Ionics **35**, 323 (1989).

[43]L. A. Gomez, L. D. S. Menezes, C. B. De Araújo, R. R. Gonçalves, S. J. L. Ribeiro, and Y. Messaddeq, J. Appl. Phys. **107**, 113508 (2010).

[44]Y. Guyot, A. Steimacher, M. P. Belançon, A. N. Medina, M. L. Baesso, S. M. Lima, L. H. C. Andrade, A. Brenier, A. Jurdyc, and G. Boulon, J. Opt. Soc. Am. B **28**, 2510 (2011).